Pressure Tuning of Berry Curvature in $CrGeTe_3$

G. Scharf,[1] B. Hen,[1] P. M. Sarte,[2] B. R. Ortiz,[2] G. Kh. Rozenberg,[1] S. D. Wilson,[2] and A. Ron[1]

[1] *Raymond and Beverly Sackler School of Physics and Astronomy, Tel-Aviv University, Tel Aviv, 69978, Israel*
[2] *Materials Department, University of California, Santa Barbara, California, 93106, USA*

The integrated Berry curvature is a geometric property that has dramatic implications on material properties. This study investigates the integrated Berry curvature and other scattering mechanisms through their contribution to the anomalous Hall effect in $CrGeTe_3$. The Anomalous Hall effect is absent in the insulating phase of $CrGeTe_3$ and evolves with pressure in a dome-like fashion as pressure is applied. The dome's edges are characterized by Fermi surface deformations, manifested as mixed electron and hole transport. We discuss the possibility that in $CrGeTe_3$ the integrated Berry curvature is tuned by the application of hydrostatic pressure due to its relation to the Fermi surface deformations.

arXiv:2401.09539v1 [cond-mat.str-el] 17 Jan 2024

For electrons in solids, Berry phase is a geometric property of the band structure that has dramatic implications on materials' properties [1]. It is acquired when a system is subject to a cyclic adiabatic transformation in its parameter space, and it is determined by the integrated Berry curvature. As a band-structure property, one may conjecture that dramatic changes to the Fermi surface will result in considerable changes to the Berry curvature and thus may result in variation of its integrated value. An extreme case of such a change would be the metal-insulator transition [2], where at the insulating state, there is no Fermi surface, and at the metallic state, a Fermi surface forms, which may host a nonzero integrated Berry curvature. Such effects were recently observed and understood theoretically in graphene moiré superlattices where Berry curvature features were tuned by varying the electric displacement field and carrier density [3, 4].

A common manifestation of the Berry phase in electronic transport properties is the anomalous Hall effect (AHE). The AHE is an additional contribution to the transverse resistivity (ρ_{xy}) on top of the ordinary Hall effect. It occurs in materials where time-reversal symmetry is broken in the presence of spin-orbit interaction [5]. As such, it can be probed through measurements of ρ_{xy} as a function of the magnetic field and serve as a superb probe for investigating the integrated Berry curvature of electrons in solids. We chose $CrGeTe_3$, a ferromagnetic insulator undergoing a metal-insulator transition with the application of hydrostatic pressure, as a laboratory for investigating the evolution of the integrated Berry curvature when the Fermi surface is strongly deformed.

$CrGeTe_3$ is a layered ferromagnetic insulator with a Curie temperature (T_{Curie}) of ~ 67 K [6] which has recently attracted a lot of attention. Inelastic neutron scattering suggests that $CrGeTe_3$ is a topological magnonic insulator [7] that is predicted to sustain ferromagnetism to the 2D limit [8–10]. Additionally, short-range fluctuations seem to play an important role above the transition temperature [11, 12], in great similarity to the closely related compound $CrSiTe_3$ [13–15].

Application of hydrostatic pressure changes T_{Curie} of $CrGeTe_3$. Up to 4.5 GPa, the Curie temperature decreases as pressure is applied [2, 16]. Above 4.5 GPa, T_{Curie} increases dramatically, rising from ~ 54 K to ~ 250 K at 9.1 GPa [2]. Within this pressure range, $CrGeTe_3$ undergoes a metal-insulator transition at ~ 6 GPa [2]. The coexistence of time-reversal symmetry breaking with the metal-insulator transition in a material with a high Z element (Te) makes $CrGeTe_3$ an ideal candidate to search for an evolution of the Berry curvature as the system is tuned through the metal-insulator transition.

In this letter, we demonstrate that the various contributions to the AHE in $CrGeTe_3$ can be tuned by hydrostatic pressure which at certain pressures is present also above 300 K suggesting possible enhancement of T_{Curie}. Measurements of the AHE at a wide range of hydrostatic pressures at T=2K reveal a dome-like behavior that onsets at the metal-insulator transition and is quenched towards higher pressures. The AHE dome coincides with the pressure range where Fermi surface deformations are observed through the ordinary Hall effect. We discuss a scenario where the AHE dome emerges due to the appearance of a nonzero integrated Berry curvature due to the observed Fermi surface deformation.

METHODS

To create the $CrGeTe_3$ crystals, Cr powder (99.95%, alfa), Ge powder (99.9999%), and Te lump (99.999+%) were sealed in a fused silica ampule at an approximate ratio of 1:1:8 Cr:Ge:Te. Fluxes were heated to 900°C at a rate of 200°C/hr, soaked at 900°C for 24h, and then slowly cooled down to 550°C at a rate of 2°C/h. The resulting fluxes were centrifuged at 550°C to remove molten Te from the crystals, after which thin platelets of dimensions 1mm x 2mm x 0.1mm were mechanically isolated.

The pressure was exerted on the samples using miniature diamond anvil cells (DACs) [17], with diamond anvil culets of 300 μm. A rhenium gasket was drilled, then filled and covered with a powder layer of 75% Al_2O_3 and 25% NaCl for electrical insulation. Two pressure cells were loaded with ~ 5 μm thick $CrGeTe_3$ flakes and placed on

top of the insulating layer, which functions as a pressure-transmitting medium. A ~ 5 μm thick Pt foil was cut into triangular pieces and placed in contact with the $CrGeTe_3$ flakes allowing electrical transport measurements at elevated pressures in the Van der Pauw geometry. As such, the ρ_{xx} and ρ_{xy} are inferred from the measured resistance up to a factor of order unity due to uncertainties in the sample geometry and thickness, which are inevitable inside a DAC. In addition, Ruby fragments were placed between the Pt leads for pressure determination [18]. The samples were compressed in steps of $2-4$ GPa and then cooled down from ambient temperature to 2 K. Measurements from the two cells are shown in this manuscript.

RESULTS AND DISCUSSION

Figure 1(a) shows that gradual application of pressure results in a significant drop to the sample resistance, which begins to saturate at pressures of ~ 6 GPa where a metal-insulator transition occurs in agreement with Ref. [2, 19] (see sections S1 and S4 in the supplementary material for resistivity versus temperature plots). T_{Curie} as a function of pressure from our AHE at high temperatures, is also shown in Figure 1(a) and will be discussed later in this section. We note that the pressure in which we observe the metal-insulator transition, and the dependence of Curie temperatures on pressure, are consistent with previous reports, indicating the similarity in sample quality and pressure conditions.

The inset of Figure 1(a) shows the Hall coefficient as a function of pressure at T = 2 K, which exhibits a dome-like behavior as a function of pressure. In the metallic state (at $6 < P < 14.5$ GPa), the negative sign of the Hall coefficient indicates that transport is electron-dominated at all temperatures, as it is demonstrated for 10.6 GPa in Figure 1(b). The full data set is available in section S5. Figure 1(c) shows that at the edges of the dome, both electrons and holes contribute to transport, as can be seen by the flattening and sign change of the Hall slope as a function of temperature. We note that a similar behavior also occurs at other pressures in the vicinity of 14 GPa, as shown in supplementary sections S5 and S6. These most likely originate from hole-like Te 5p and electron-like Cr 3d bands. It should be mentioned that measurements of the Hall effect were infeasible at pressures below 3.2 GPa due to the large longitudinal resistivity relative to the magnitude of the Hall effect (supplementary material section S6).

Above 5.6 GPa, when $CrGeTe_3$ enters the metallic state, a significant AHE signal is observed. Figure 2(a) shows a characteristic behavior of the AHE in the intermediate pressure regime. Here, the AHE is the strongest at low temperatures and monotonically weakens as the temperature increases. From this data, it is clear that the

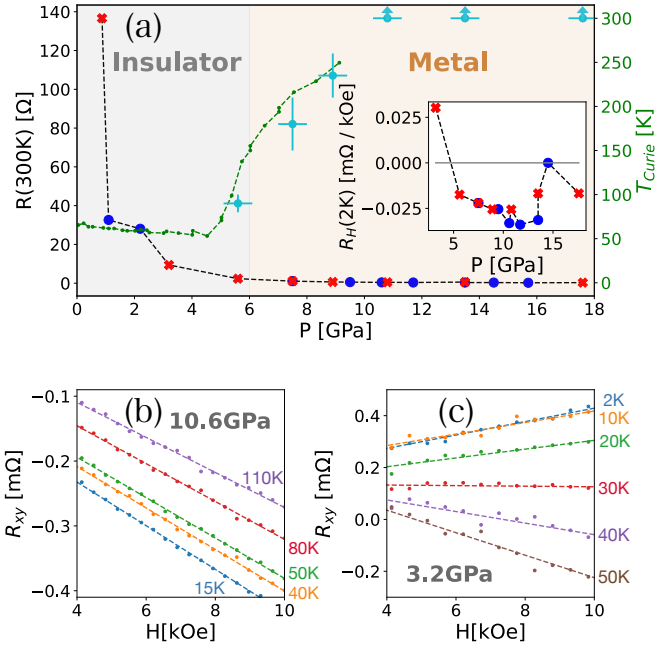

FIG. 1. The left axis of the panel (a) shows a significant decrease in the samples' resistance as pressure is applied due to the metal-insulator transition. The Blue and red points represent measurements from cells 1 and 2, respectively. The values are scaled by a single geometric factor of order unity, which is used throughout the manuscript for any longitudinal resistivity measurement. On the right axis, we show the Curie temperature as a function of applied pressure. The cyan dots represent measurements from this work based on the AHE, which extend the pressure range covered in Ref. [2], shown in green. The uncertainties in the value of T_{Curie} are estimated as the interval between our sampling points, and the pressure uncertainties are estimated to be about 0.5 GPa. The arrows signify that the value of 300 K is a lower bound for the Curie point, as it is the highest temperature in which data was taken. The inset shows the Hall coefficient as a function of applied pressure at 2 K extracted from a linear fit in the field range between 4 kOe and 10 kOe. The Blue and the red points are measurements of ρ_{xy} from the first and second cells, respectively. A single geometric factor of order unity was used to scale the values of ρ_{xy} here and throughout the manuscript. Panels (b) and (c) show the antisymmetrized Hall measurements at pressures of 10.6 GPa and 3.2 GPa at different temperatures as a function of the magnetic field at the range which was used to calculate the Hall coefficient.

AHE persists to much higher temperatures than the Curie temperature (T_{Curie}) under ambient pressure (~ 67 K), which we interpret as an increase of T_{Curie}. We note that the AHE can also occur in paramagnetic materials [20, 21], and therefore its presence at high temperatures does not necessarily signify enhancement of T_{Curie}. However, we find this scenario less likely since the trend observed by our measurements is a smooth continuation of the trend observed by magnetometry measurements [2] shown in Figure 1(a). Figure 2(b) shows measurements of the AHE at 13.5 GPa, characteristic of the high-pressure regime

between 13.5 and 17.6 GPa. At low temperatures (blue curves), the AHE is completely absent from measurements of ρ_{xy}, as can be seen by the absence of the steep low field AHE slope. As the temperature increases, the AHE gradually appears and is enhanced at elevated temperatures. We note that the AHE does not decay even at room temperature, continuing the trend observed in Ref. [2], thus possibly indicating that T_{Curie} in $CrGeTe_3$ surpasses room temperature at this pressure range.

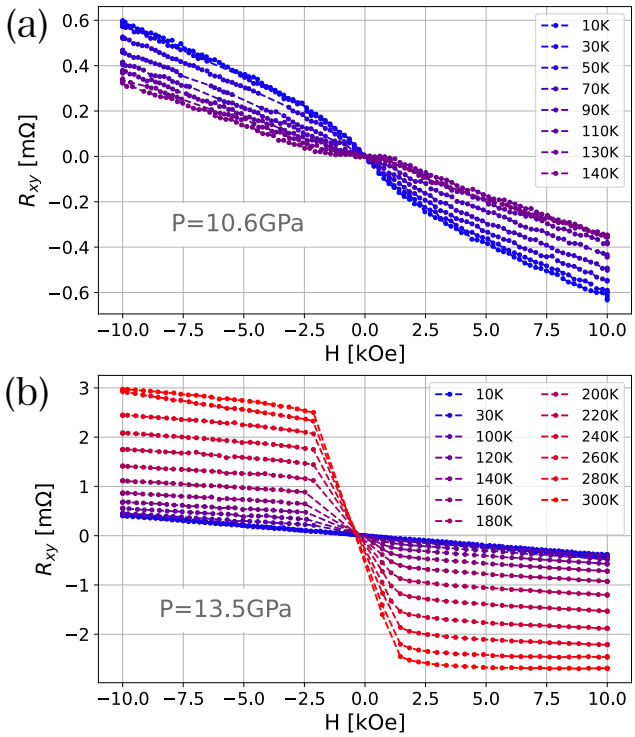

FIG. 2. Measurements of the Hall effect in sample 1 at different temperatures at pressures of 10.6 GPa (panel (a)) and 13.5 GPa (panel (b)). The steep slopes at low fields are due to the AHE.

The qualitative differences in the evolution of the AHE with temperature suggest that different mechanisms are at play in different pressure regimes. To disentangle the contributions to the AHE, we separate the anomalous Hall resistivity ρ_{AHE} to intrinsic and extrinsic sources and follow Hou *et al.* [22] who further distinguish between extrinsic scattering originating from static (temperature independent) and dynamic (temperature dependent) scattering mechanisms. At low temperatures, quasiparticles are frozen, and there are no dynamic scattering events. Therefore, $\rho_{AHE}(T = 0)$ is a static effect, either intrinsic with geometric origins or extrinsic emanating from disorder. At higher temperatures, quasiparticles are thermally activated and dynamic extrinsic scattering mechanisms may contribute to the AHE. We turn to interpret our results in light of these distinctions in the three pressure regimes.

ρ_{AHE} is extracted using a procedure similar to Ref. [23] detailed in the supplementary section S3. In the insulating state, the values of the longitudinal resistance (R_{xx}) intermixed in the measurements of R_{xy} are dominant for fields smaller than 0.2 T (see section S6 in the supplementary material). Therefore, our measurements are insensitive to small anomalous Hall signals at this pressure range. Figure 3 shows ρ_{AHE} as a function of temperature for various pressures above 5.6 GPa. At the intermediate pressure regime, at low temperatures, $\rho_{AHE} \neq 0$. This suggests that the pressure tuning into the metallic state activates either an intrinsic contribution to the AHE or a static extrinsic scattering mechanism. The signal decays as the temperature increases, and its disappearance marks the Curie temperature. In the high-pressure regime (P > 13.5 GPa), $\rho_{AHE} = 0$ at low temperatures and smoothly increases as the temperature increases, persisting up to room temperature above which we could not heat our DACs. The absence of AHE indicates either a perfect cancellation of contributions from various scattering mechanisms, meaning that the sum of all the various contributions to the AHE is zero, or the complete nullification of all of them. Perfect cancellation typically occurs when two mechanisms contribute to ρ_{AHE} with opposite signs, which typically occurs at a specific temperature as seen, for example, in Ref. [24–27]. In contrast, in $CrGeTe_3$ at P > 13 GPa, $\rho_{AHE} = 0$ at a wide temperature range (over 150 K at 17.6 GPa) rather than crossing zero at a particular temperature. Perfect accidental cancellation of various scattering mechanisms at such a wide temperature range is unlikely. Therefore we deduce that for P > 13 GPa, all scattering mechanisms are negligible at low temperatures, and the behavior shown in Figure 3 is dominated by scattering off of thermally activated quasi-particles.

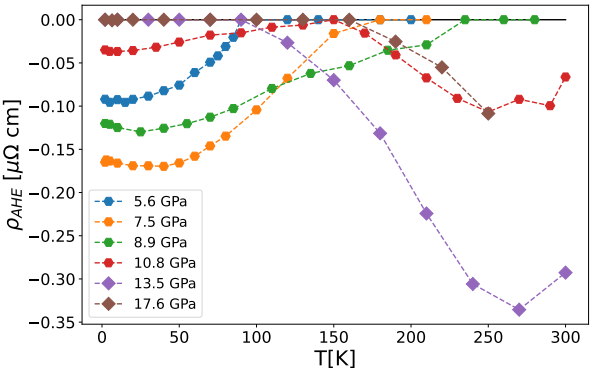

FIG. 3. ρ_{AHE} as a function of temperature for various pressures, measured in sample 2. A similar plot for sample 1 is shown in S2 in the supplementary material. At the intermediate pressure regime, between the metal-insulator transition and 13 GPa, $\rho_{AHE} \neq 0$ at low temperatures and decays smoothly as the temperature increases. In contrast, in the high-pressure regime, at low temperatures $\rho_{AHE} = 0$, and increases as the temperature increases.

In Figure 4, we plot ρ_{AHE} at 2 K as a function of the pressure, which exhibits a dome-like shape starting at the metal-insulator transition and finishing around 13 GPa. To the best of our knowledge, this behavior has not been observed in the past. Typically, ferromagnets exhibit a monotonic behavior of the AHE as a function of pressure, as seen, for example, in CeAlSi [28] and $Co_3Sn_2S_2$ [29], where in the former, the AHE is generated by skew scattering and in the latter by the intrinsic Berry phase. To understand this behavior, we look at the relation between ρ_{AHE} and ρ_{xx}, which at low temperatures, in the absence of dynamic scattering, simplifies to [22]:

$$\rho_{AHE} = \alpha\rho_{xx} + \beta_0\rho_{xx}^2 \tag{1}$$

where α represents contributions from skew scattering, and β_0 is a mixture of intrinsic and static side jump mechanisms. In our experiment, we tune ρ_{xx} by changing the hydrostatic pressure P. The inset to Figure 4 shows ρ_{AHE} as a function of $\rho_{xx}(P)$ at a constant temperature T = 2 K, where a clear non-parabolic hysteretic behavior is observed. This means that the application of pressure changes not only ρ_{xx} but also α and β_0. Transport measurements alone could not disentangle the contributions of the intrinsic and the static extrinsic mechanisms to the AHE. However, in $CrGeTe_3$, the AHE dome onsets and ends in regimes where mixed transport of electrons and holes is observed (Figure 1(a) inset), indicative of Fermi surface deformations. We suggest that the Fermi surface deformations result in the appearance of nonzero integrated Berry curvature, which is in some similarity to what has been observed in graphene moiré superlattices [3, 4]. Generally, the intrinsic contribution to the AHE depends on the integrated Berry curvature over all occupied states [1]. Therefore, it can be tuned by either changing the Fermi level or by causing changes to the band structure that manifest changes to the Berry curvature. A toy model calculation, based on Ref [30], where the integrated Berry curvature is tuned by changing the Fermi energy can be found in Ref [1]. Similar phenomena were observed experimentally and understood theoretically in graphene moiré superlattices, where both the band structure and the Fermi level were changed[3, 4]. We suggest that in $CrGeTe_3$, at the metal-insulator transition, the effects of nonzero integrated Berry's curvature appear, contributing to ρ_{AHE} at low temperatures. As pressure increases, those effects get stronger due to the hybridization of the Te and the Cr bands, which mark the rising part of the AHE dome. As the pressure further increases, the AHE weakens and goes to zero at the point where mixed electron/hole transport is observed again. We note that at the end of the AHE dome, structural anomalies were observed by x-ray diffraction as nonmonotonic behavior of the ∠Te-Cr-Te angle [19]. In light of the nonmonotonic behavior of atomic positions, one may not be surprised by the nonmonotonic behavior we report in the electronic properties of $CrGeTe_3$. Additionally, Dong and coauthors [31] observed a kink in the axial ratio at 14 GPa in $CrGeTe_3$ and claim it is indicative of an isostructural phase transition, which is possibly related to the mixed electron-hole transport we observe. It is worth noting that the behavior depicted in Figure 4 can also be explained through changes in the skew-scattering and static side jumps contributions to the AHE as a function of the pressure. However, since the AHE dome onsets at the metal-insulator transition and ends where another Fermi surface deformation was observed strengthens our belief that the observed dome-like behavior of the AHE at low temperatures is due to changes in the integrated Berry's curvature tuned by the application of hydrostatic pressure.

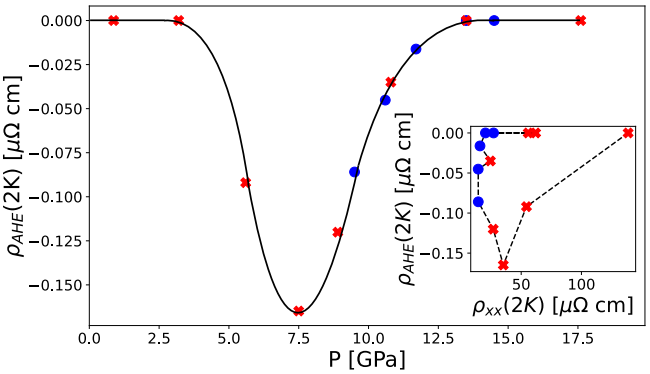

FIG. 4. ρ_{AHE} measured at 2 K as a function of applied pressure. The black line is a guide to the eye. The inset shows ρ_{AHE}, measured at 2 K, as a function of the longitudinal resistivity ρ_{xx}, showing a hysteretic behavior that deviates from the parabolic relation in equation 1. The Blue and the red points are from the first and second cells, respectively. Their resistivity values are scaled by a single geometric factor of order unity, as was previously mentioned in Figure 1.

In summary, we have measured the AHE in $CrGeTe_3$ as a function of applied hydrostatic pressure and temperature. We suggest that the application of hydrostatic pressure to $CrGeTe_3$ results in the tuning of the intrinsic contribution to the AHE, which originates from nonzero integrated Berry's curvature in proximity to the metal-insulator transition and a Fermi surface deformation. We also found that at elevated pressures, the AHE appears at temperatures above 300 K suggestive of possible enhancement of T_{Curie}, continuing and agreeing with the trend observed by Bhoi *et al.* [2].

A. R. acknowledges support from the Zuckerman Foundation, and the Israel Science Foundation (Grant No. 1017/20). S.D.W., B.R.O., and P.S. gratefully acknowledge support via the UC Santa Barbara NSF Quantum Foundry funded via the Q-AMASE-i program under award DMR-1906325. G. Kh. R. acknowledges the Israel Science Foundation (Grants No. 1748/20). G. S. thanks Shay Sandik, Itai Silber, and Gal Tuvia for the help with the cryogenic equipment.

[1] D. Xiao, M.-C. Chang, and Q. Niu, Rev. Mod. Phys. **82**, 1959 (2010) .

[2] D. Bhoi, J. Gouchi, N. Hiraoka, Y. Zhang, N. Ogita, T. Hasegawa, K. Kitagawa, H. Takagi, K. H. Kim, and Y. Uwatoko, Physical Review Letters **127**, 217203 (2021) .

[3] S. Sinha, P. C. Adak, A. Chakraborty, K. Das, K. Debnath, L. V. Sangani, K. Watanabe, T. Taniguchi, U. V. Waghmare, A. Agarwal, *et al.*, Nature Physics **18**, 765 (2022) .

[4] M. Kuiri, C. Coleman, Z. Gao, A. Vishnuradhan, K. Watanabe, T. Taniguchi, J. Zhu, A. H. MacDonald, and J. Folk, Nature Communications **13**, 6468 (2022) .

[5] N. Nagaosa, J. Sinova, S. Onoda, A. H. MacDonald, and N. P. Ong, Reviews of modern physics **82**, 1539 (2010) .

[6] V. Carteaux, D. Brunet, G. Ouvrard, and G. Andre, Journal of Physics: Condensed Matter **7**, 69 (1995) .

[7] F. Zhu, L. Zhang, X. Wang, F. J. Dos Santos, J. Song, T. Mueller, K. Schmalzl, W. F. Schmidt, A. Ivanov, J. T. Park, *et al.*, Science advances **7**, eabi7532 (2021) .

[8] X. Li and J. Yang, Journal of Materials Chemistry C **2**, 7071 (2014) .

[9] C. Xu, J. Feng, H. Xiang, and L. Bellaiche, npj Computational Materials **4**, 1 (2018) .

[10] H. L. Zhuang, Y. Xie, P. Kent, and P. Ganesh, Physical Review B **92**, 035407 (2015) .

[11] L. Chen, C. Mao, J.-H. Chung, M. B. Stone, A. I. Kolesnikov, X. Wang, N. Murai, B. Gao, O. Delaire, and P. Dai, Nature communications **13**, 1 (2022) .

[12] G. Lin, H. Zhuang, X. Luo, B. Liu, F. Chen, J. Yan, Y. Sun, J. Zhou, W. Lu, P. Tong, *et al.*, Physical Review B **95**, 245212 (2017) .

[13] A. Ron, E. Zoghlin, L. Balents, S. Wilson, and D. Hsieh, Nature communications **10**, 1 (2019) .

[14] A. Ron, S. Chaudhary, G. Zhang, H. Ning, E. Zoghlin, S. Wilson, R. Averitt, G. Refael, and D. Hsieh, Physical Review Letters **125**, 197203 (2020) .

[15] T. J. Williams, A. A. Aczel, M. D. Lumsden, S. E. Nagler, M. B. Stone, J.-Q. Yan, and D. Mandrus, Physical Review B **92**, 144404 (2015) .

[16] T. Sakurai, B. Rubrecht, L. Corredor, R. Takehara, M. Yasutani, J. Zeisner, A. Alfonsov, S. Selter, S. Aswartham, A. Wolter, *et al.*, Physical Review B **103**, 024404 (2021) .

[17] E. Sterer, M. Pasternak, and R. Taylor, Review of scientific instruments **61**, 1117 (1990) .

[18] A. Dewaele, M. Torrent, P. Loubeyre, and M. Mezouar, Phys. Rev. B **78**, 104102 (2008) .

[19] Z. Yu, W. Xia, K. Xu, M. Xu, H. Wang, X. Wang, N. Yu, Z. Zou, J. Zhao, L. Wang, *et al.*, The Journal of Physical Chemistry C **123**, 13885 (2019) .

[20] D. Maryenko, A. Mishchenko, M. Bahramy, A. Ernst, J. Falson, Y. Kozuka, A. Tsukazaki, N. Nagaosa, and M. Kawasaki, Nature communications **8**, 1 (2017) .

[21] D. Culcer, A. MacDonald, and Q. Niu, Phys. Rev. B **68**, 045327 (2003) .

[22] D. Hou, G. Su, Y. Tian, X. Jin, S. A. Yang, and Q. Niu, Physical review letters **114**, 217203 (2015) .

[23] E. Liu, Y. Sun, N. Kumar, L. Muechler, A. Sun, L. Jiao, S.-Y. Yang, D. Liu, A. Liang, Q. Xu, *et al.*, Nature physics **14**, 1125 (2018) .

[24] Z. Fang, N. Nagaosa, K. S. Takahashi, A. Asamitsu, R. Mathieu, T. Ogasawara, H. Yamada, M. Kawasaki, Y. Tokura, and K. Terakura, Science **302**, 92 (2003) .

[25] P. Pureur, F. W. Fabris, J. Schaf, and I. A. Campbell, Europhysics Letters **67**, 123 (2004) .

[26] C. Zeng, Y. Yao, Q. Niu, and H. H. Weitering, Phys. Rev. Lett. **96**, 037204 (2006) .

[27] N. Haham, Y. Shperber, M. Schultz, N. Naftalis, E. Shimshoni, J. W. Reiner, and L. Klein, Physical Review B **84**, 174439 (2011) .

[28] M. M. Piva, J. C. Souza, V. Brousseau-Couture, S. Sorn, K. R. Pakuszewski, J. K. John, C. Adriano, M. Côté, P. G. Pagliuso, A. Paramekanti, and M. Nicklas, Phys. Rev. Res. **5**, 013068 (2023) .

[29] Z. Liu, T. Zhang, S. Xu, P. Yang, Q. Wang, H. Lei, Y. Sui, Y. Uwatoko, B. Wang, H. Weng, *et al.*, Physical Review Materials **4**, 044203 (2020) .

[30] S. Onoda, N. Sugimoto, and N. Nagaosa, Phys. Rev. Lett. **97**, 126602 (2006) .

[31] E. Dong, B. Liu, Q. Dong, X. Shi, X. Ma, R. Liu, X. Zhu, X. Luo, X. Li, Y. Li, *et al.*, Physica B: Condensed Matter **595**, 412344 (2020) .

SUPPLEMENTAL MATERIAL

S1 - The MIT - R(T) at different pressures

The longitudinal resistance as a function of temperature, normalized at 9.5 K, measured at different pressures in the first cell. The change in the behavior of the graph from decreasing to increasing as a function of the temperature in the low-temperature regime by application of pressure indicates a metal-insulator transition driven by the application of pressure on the $CrGeTe_3$.

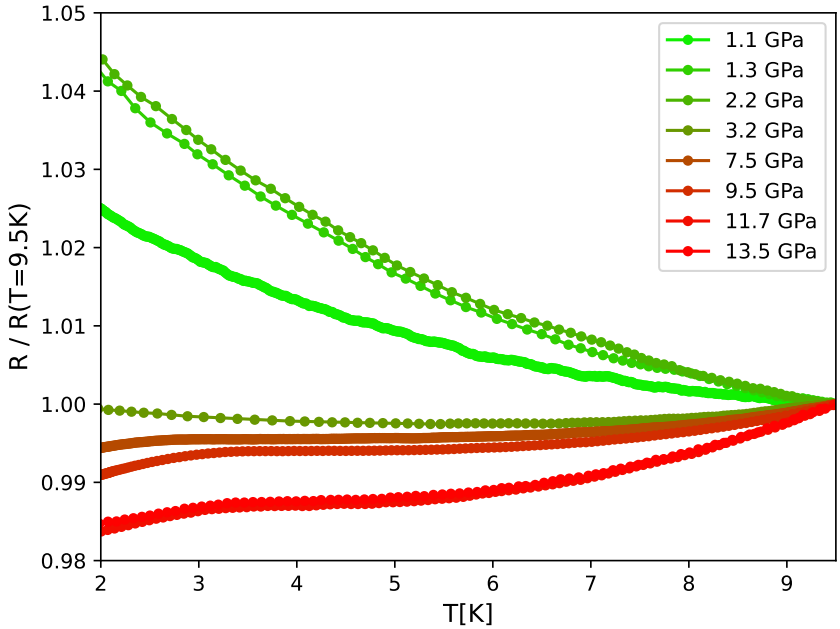

FIG. S1. The longitudinal resistance as a function of temperature, normalized at 9.5 K, measured at different pressures in the first cell. The change in the behavior of the graph from decreasing to increasing as a function of the temperature by application of pressure indicates a MIT driven by the application of pressure on the $CrGeTe_3$.

S2 - THE AHE measured in the first cell

Here we present our measurements of ρ_{AHE} as a function of temperature for the various pressures measured in the first sample. As was also observed in the second sample (in the main text), At pressures below 13 GPa, $\rho_{AHE} \neq 0$ at low temperatures and decays smoothly as the temperature increases. In contrast, for P > 13 GPa, at low temperatures $\rho_{AHE} = 0$, and increases as the temperature increases.

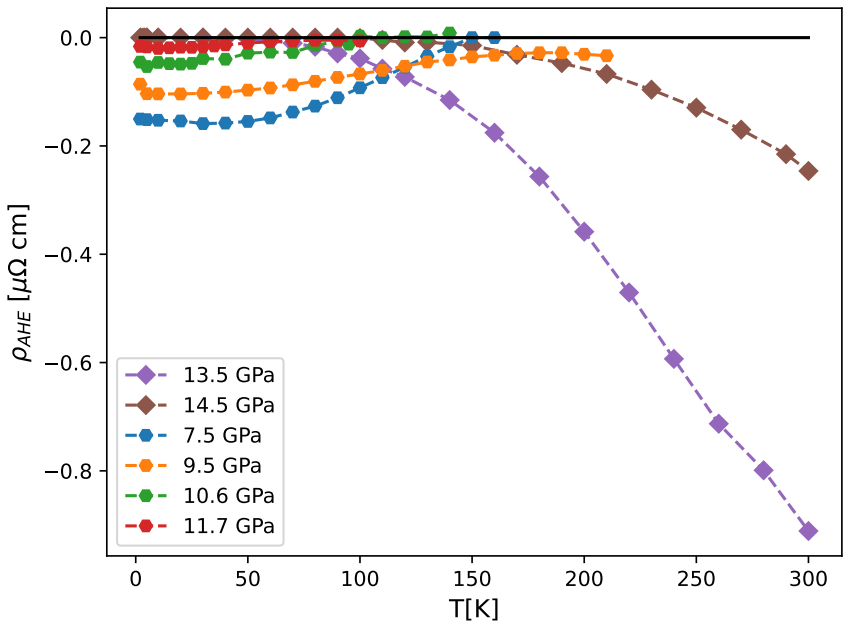

FIG. S2. ρ_{AHE} as a function of temperature for the various pressures measured for sample 1.

S3 - The extraction of ρ_{AHE} from the measurements

ρ_{AHE} in a specific temperature and pressure, is extracted from the measurements by measuring $R_{xy}(H)$ and antisymmetrize it. This results in graphs as shown in section S6. Then we do a linear fit to the high-field regime (4 kOe < H), and the intersection of the fit with the y-axis is the AHE resistance (R_{AHE}) (see Fig.S3). Finally, by multiplying R_{AHE} with the width of the sample, we get ρ_{AHE}.

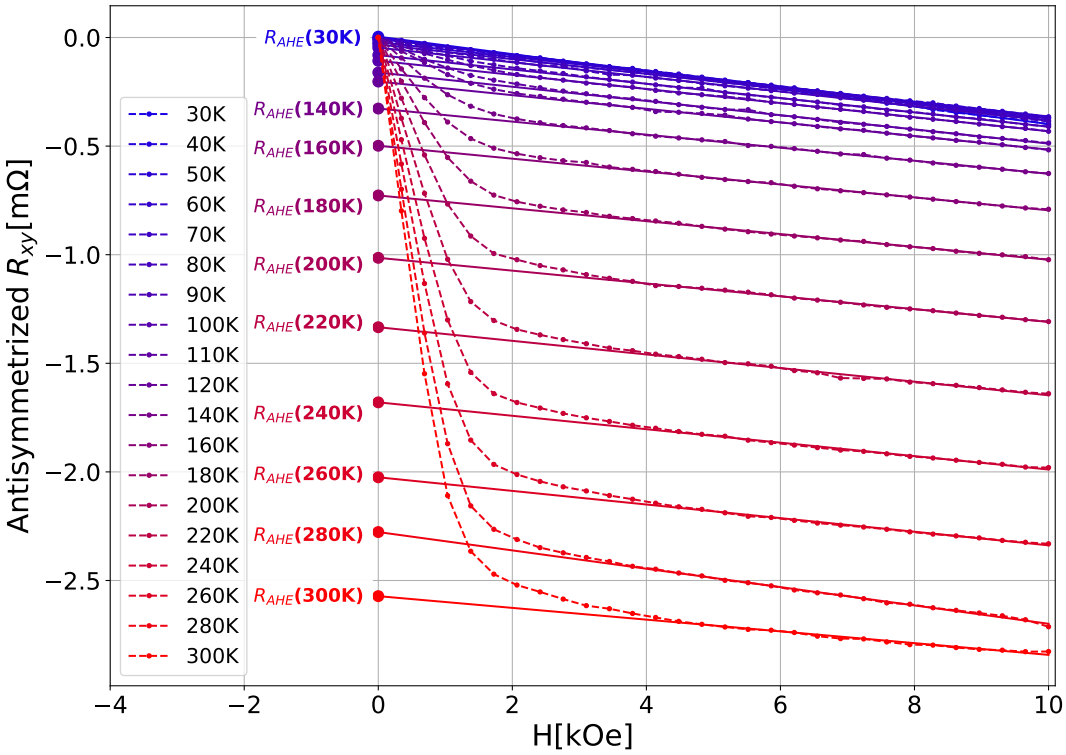

FIG. S3. Here we show an example of how we extracted the AHE resistance (R_{AHE}) for each pressure at different temperatures. The figure displays the antisymmetrization of the raw data of R_{xy} as a function of the applied field H, measured at several different temperatures for the first sample in the metallic state at a pressure of 13.5 GPa. The solid lines are the linear fit for the high-fields regime (4 kOe < H) at each temperature, and the big dots represent the intersection of each fit with the y-axis. The intersection of each fit is R_{AHE} measured at each temperature.

S4 - ρ_{xx} at different pressures an temperatures

In Figure S5, we present the longitudinal resistivity as a function of temperature in the metallic state, measured on both samples. As can be seen, they show very similar behavior as all of them are monotonic - increasing with the temperature and showing similar values. As such, going back to our measurements of the AHE as a function of the temperature (see Figures 2 and S2), the observed behaviors cannot be explained just by the scaling of ρ_{AHE} with the ρ_{xx}. First, the scaling of ρ_{xx} cannot explain the change in the behavior of the AHE between the intermediate pressure regime (5.6 GPa < P < 13 GPa) and the high-pressure regime (13 Gpa < P). Second, it cannot explain why at 13.5 GPa, the AHE is stronger than at higher pressures in the first sample and thus probably not also in the second cell. Finally, going back to the low-temperature behavior of the AHE as shown in Figure 4, the values of ρ_{xx} at low temperatures (shown in log-scale in Figure S6) cannot explain the dome-like behavior of the AHE.

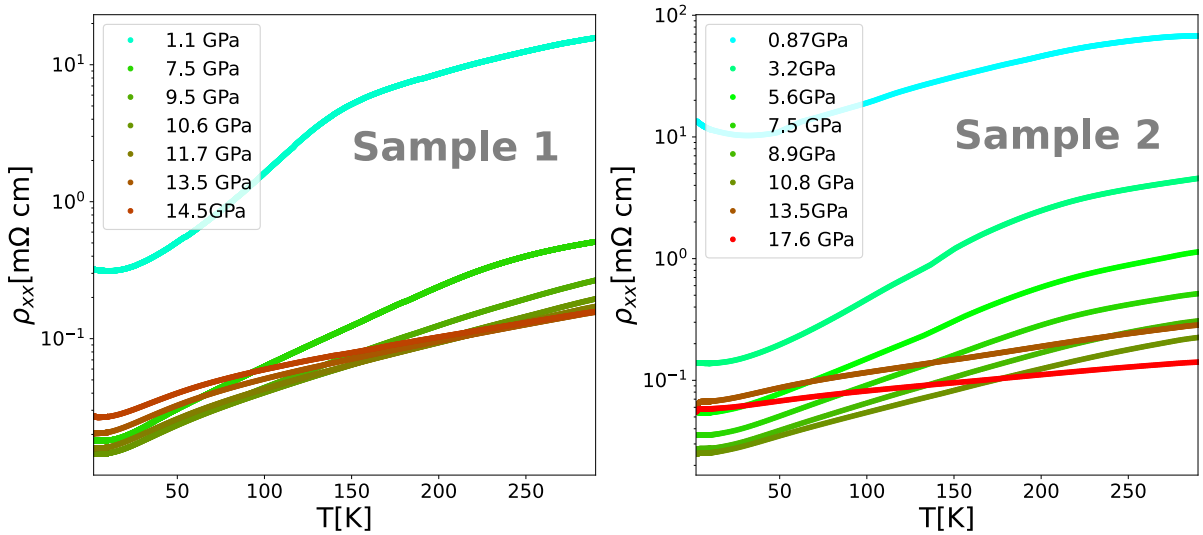

FIG. S4. The longitudinal resistivity as a function of temperature at different pressures presented in log-scale, on the left in the first sample and on the right in the second sample.

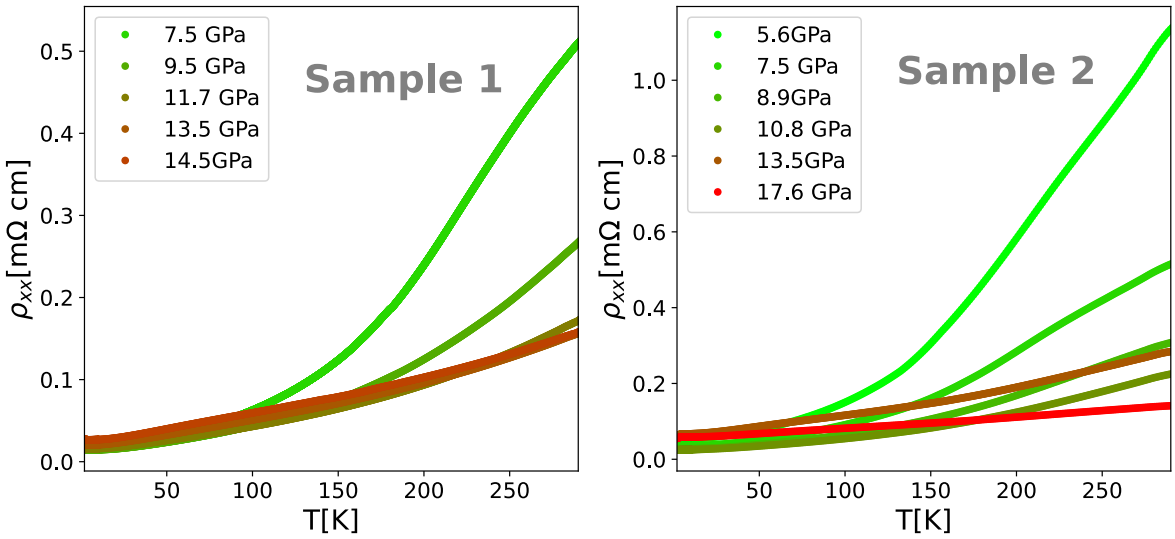

FIG. S5. The longitudinal resistivity as a function of temperature at different pressures in the metallic state, on the left in the first sample and on the right in the second sample.

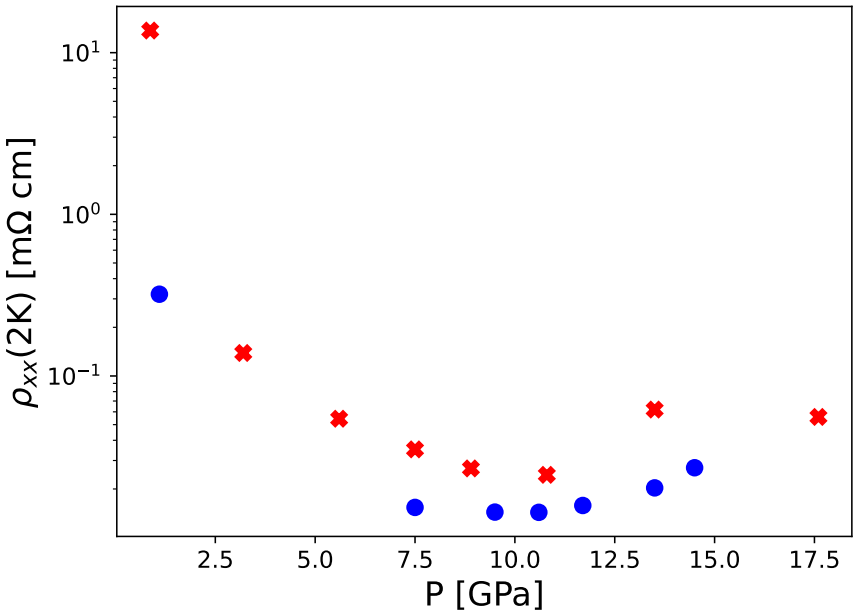

FIG. S6. The longitudinal resistivity at low temperature (2K) as a function of the pressure in log-scale. The Blue and the red points are from the first and second cells, respectively. Their resistivity values are scaled by a single geometric factor of order unity which was used throughout the manuscript for each longitudinal measurement.

S5 - The Hall slopes measured at different pressures and temperatures

Here, we present the Hall slopes as a function of temperature, measured at different pressures. In most measurements, the Hall slope is negative, meaning that although there is a mix of electrons and holes in all pressures, in most of the pressures, we can treat the transport as of electron-like charge carriers. However, at 3.2 GPa and at 14.5 GPa, there is a change in the sign of the Hall slope, indicating that these pressures, both holes and electrons contribute to the transport where their contributions are temperature dependent, which can be seen in Figure 1(b) in the text as well. At these pressures, we cannot treat the transport as dominated by a single charge carrier. The fact that the Hall slope changes sign as a function of the temperature at those pressures but not before might indicate changes in the band structure of the $CrGeTe_3$, which may result in a change in the integrated Berry curvature.

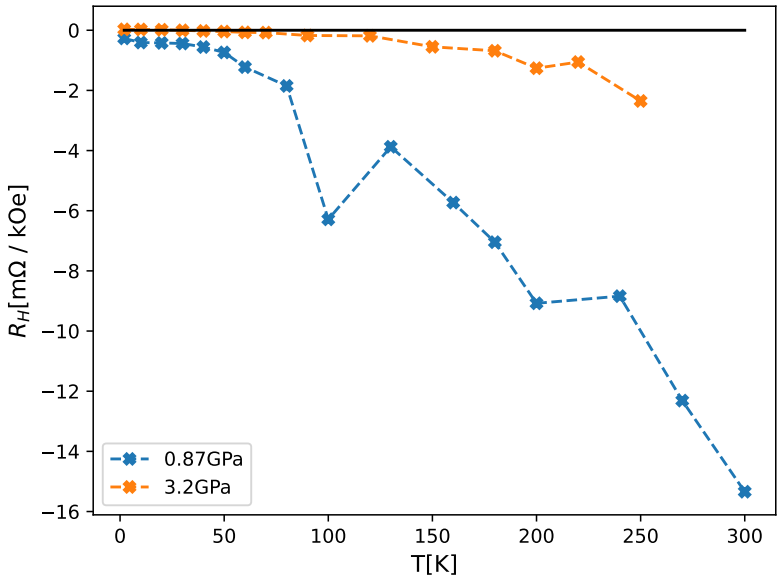

FIG. S7. The Hall slopes as a function of temperature, measured at 0.87 GPa and at 3.2 GPa.

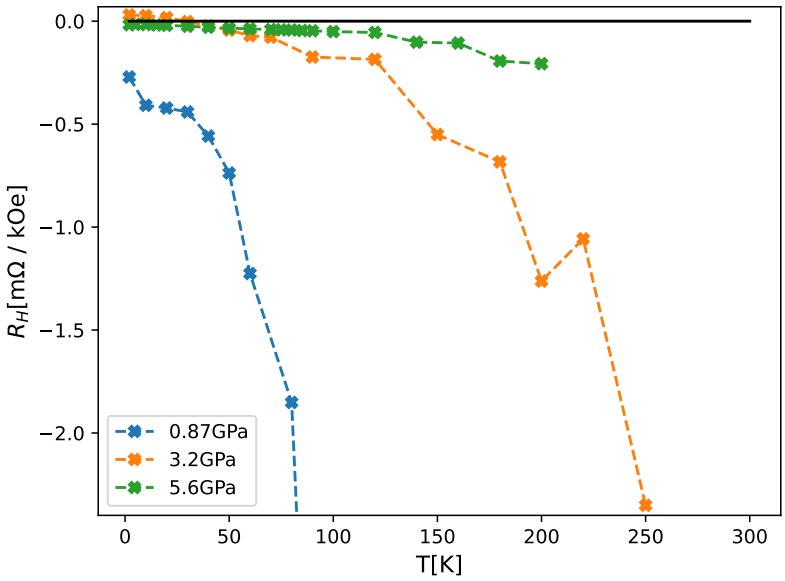

FIG. S8. The Hall slopes as a function of temperature, measured at 0.87 GPa, 3.2 GPa, and 5.6 GPa.

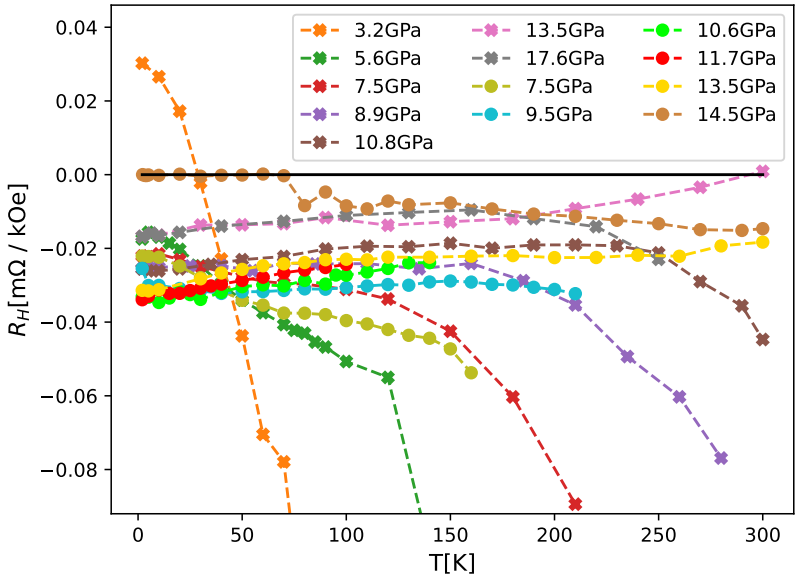

FIG. S9. The Hall slopes as a function of temperature, measured at different pressures. The dots represent data from the first cell, and the Xs denote measurements from the second cell.

S6 - Raw Data measurements of R_{xy} and the resulted anti-symmetric plots for all pressures and cells

Here we present measurements of R_{xy} as a function of the applied field H at various pressures and temperatures, both in their raw form and after undergoing antisymmetrization. When there is significant mixing of R_{xx} and R_{xy} in the measurements, it is reflected in the raw data, which appears neither symmetric nor antisymmetric. This effect has been observed multiple times, particularly in the low-pressure regime before the metal-insulator transition.

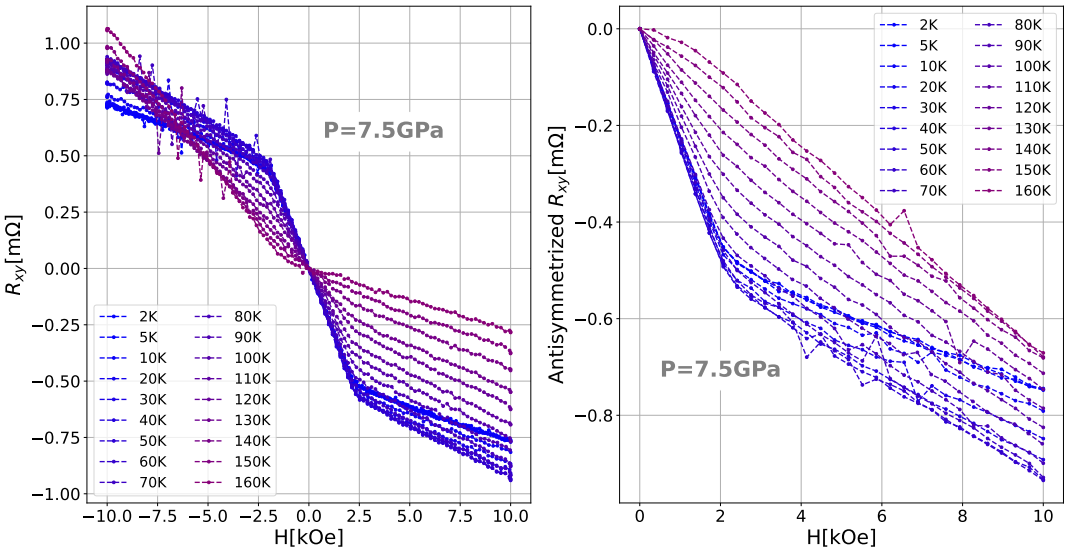

FIG. S10. The left panel displays the raw data of R_{xy} as a function of the applied field H for the first sample in the metallic state at a pressure of 7.5 GPa. The right panel shows the same data after antisymmetrization.

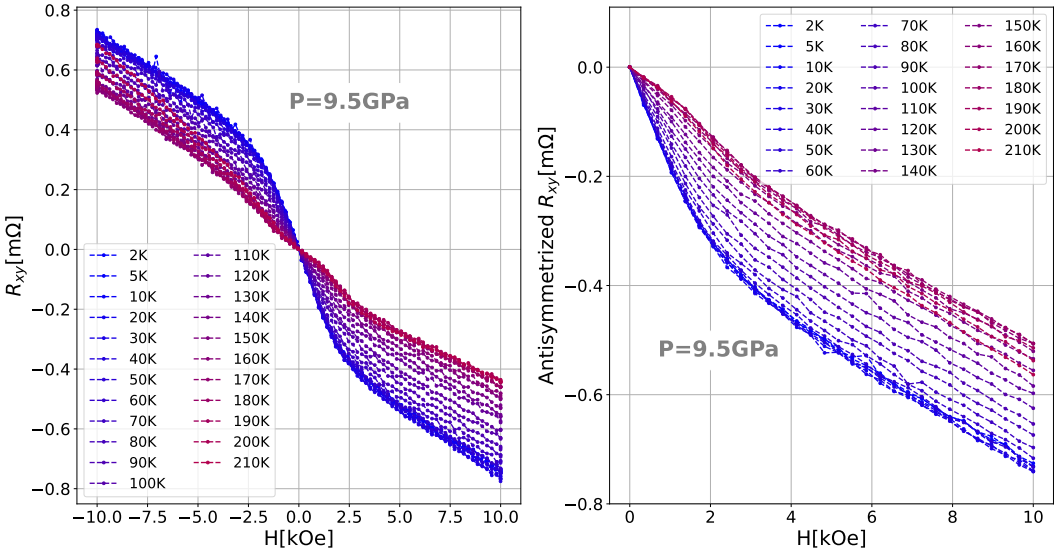

FIG. S11. The left panel displays the raw data of R_{xy} as a function of the applied field H for the first sample in the metallic state at a pressure of 9.5 GPa. The right panel shows the same data after antisymmetrization.

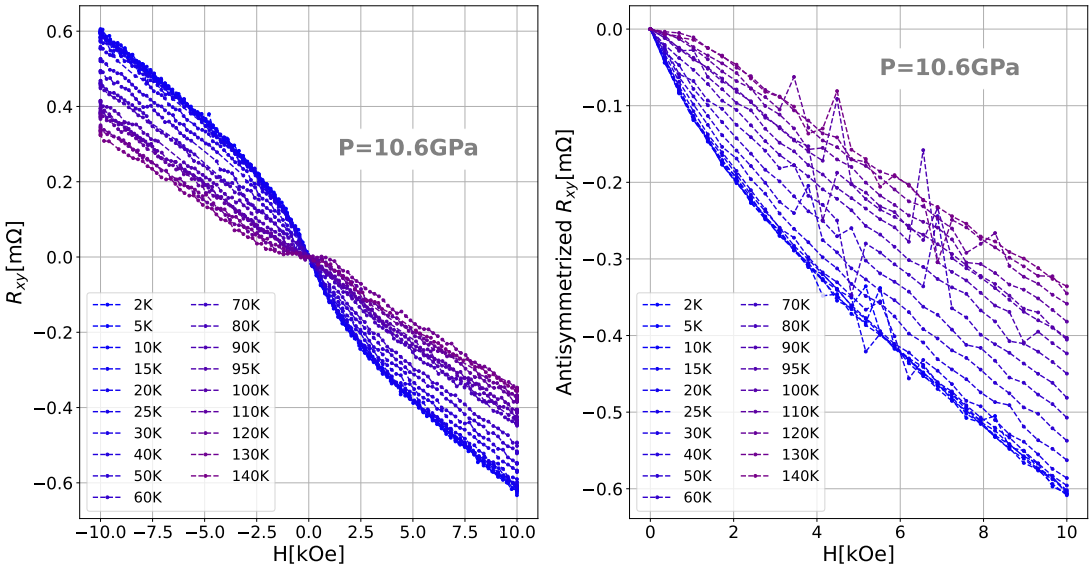

FIG. S12. The left panel displays the raw data of R_{xy} as a function of the applied field H for the first sample in the metallic state at a pressure of 10.6 GPa. The right panel shows the same data after antisymmetrization.

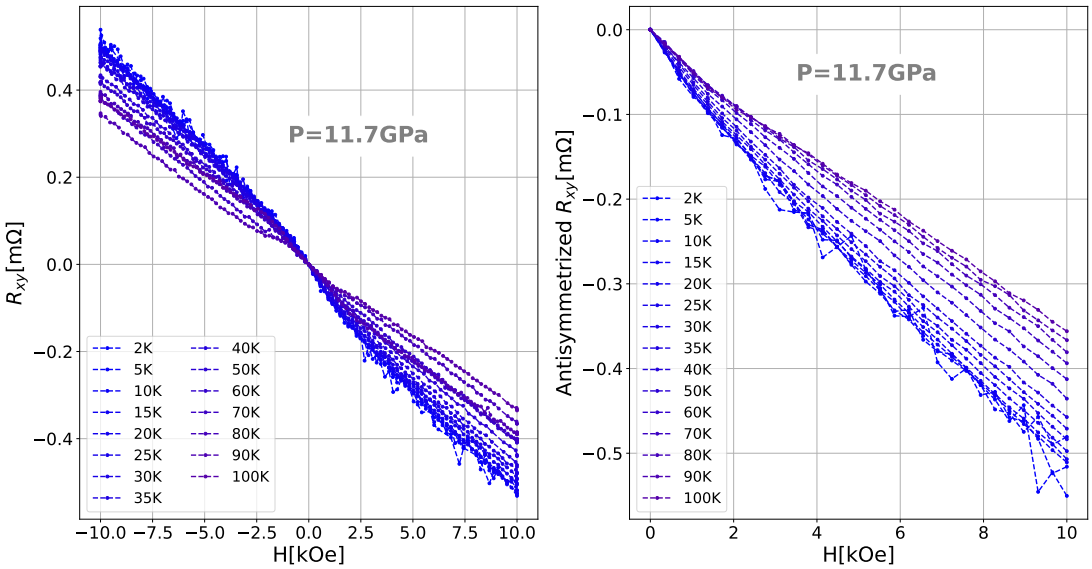

FIG. S13. The left panel displays the raw data of R_{xy} as a function of the applied field H for the first sample in the metallic state at a pressure of 11.7 GPa. The right panel shows the same data after antisymmetrization.

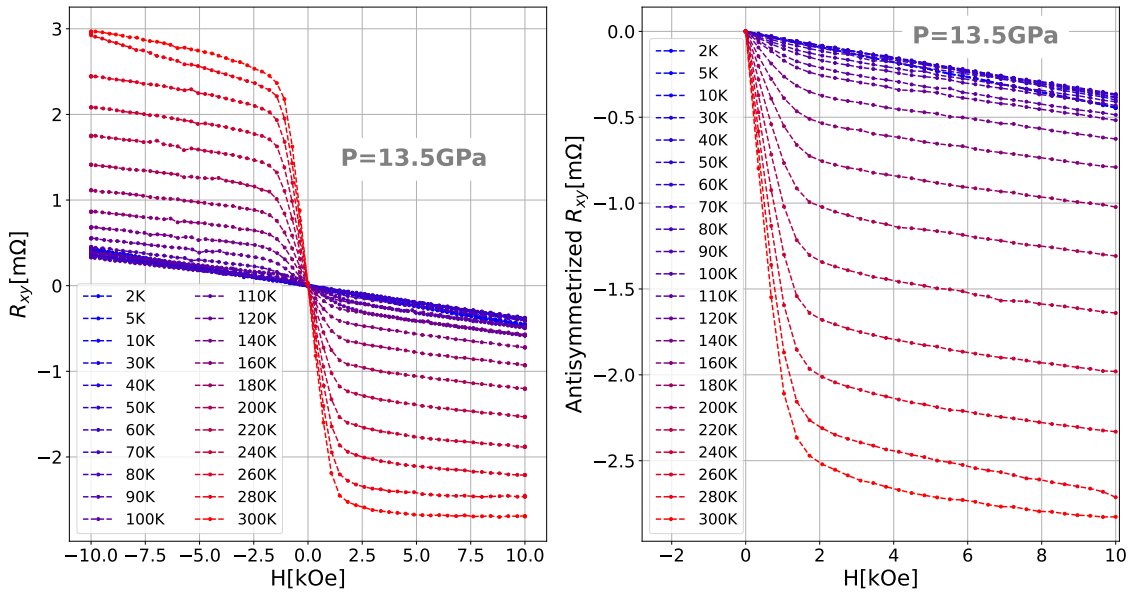

FIG. S14. The left panel displays the raw data of R_{xy} as a function of the applied field H for the first sample in the metallic state at a pressure of 13.5 GPa. The right panel shows the same data after antisymmetrization.

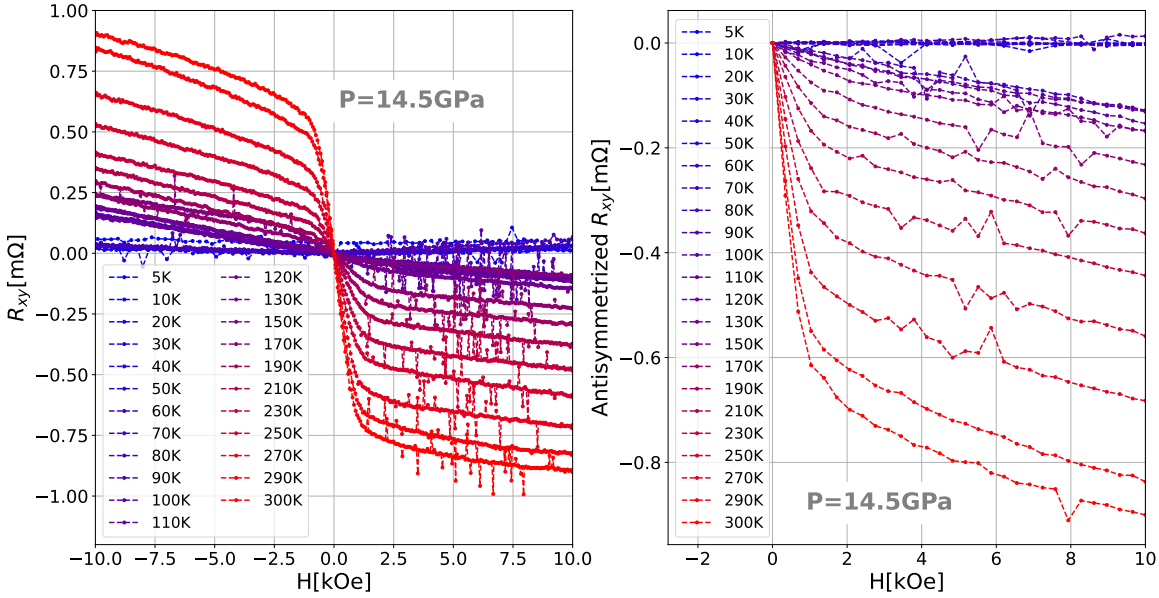

FIG. S15. The left panel displays the raw data of R_{xy} as a function of the applied field H for the first sample in the metallic state at a pressure of 14.5 GPa. The right panel shows the same data after antisymmetrization.

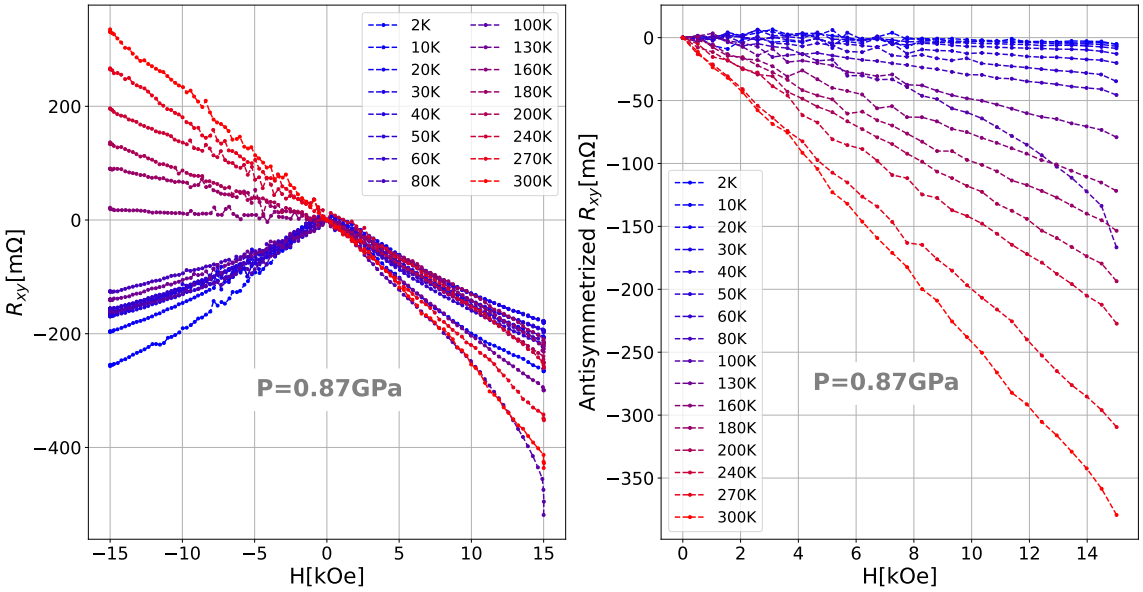

FIG. S16. The left panel displays raw data of R_{xy} as a function of the applied field H for the second sample in the insulating state at a pressure of 0.87 GPa. The right panel presents the same data after antisymmetrization. The presence of significant intermixing between R_{xx} and R_{xy} can be easily identified by the absence of symmetry or antisymmetry in the raw data.

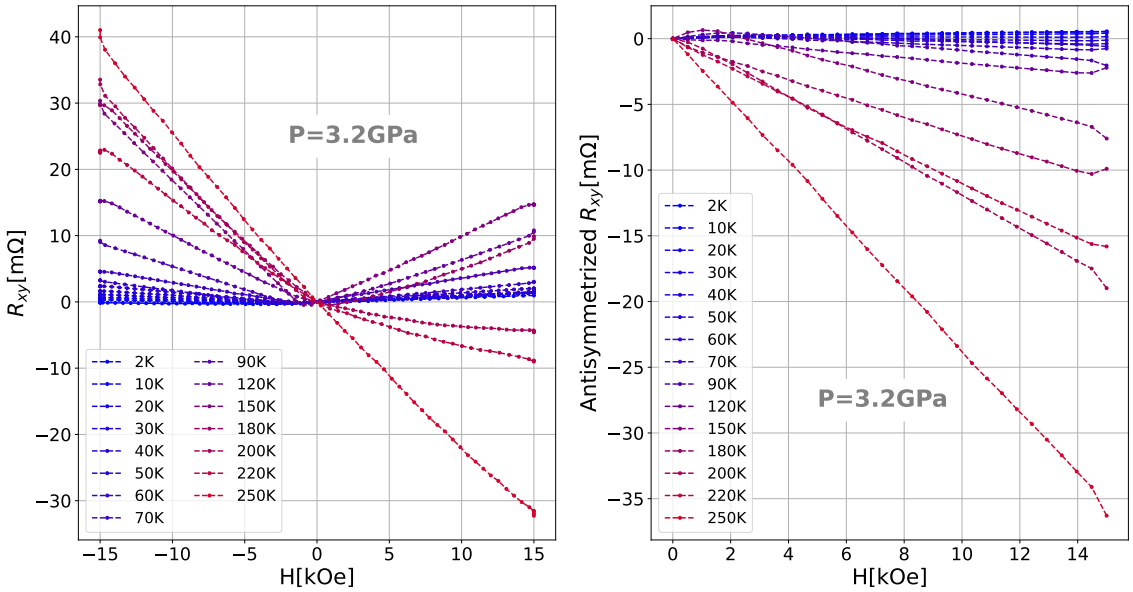

FIG. S17. The left panel displays raw data of R_{xy} as a function of the applied field H for the second sample in the insulating state at a pressure of 3.2 GPa. The right panel presents the same data after antisymmetrization. The presence of significant intermixing between R_{xx} and R_{xy} can be easily identified by the absence of symmetry or antisymmetry in the raw data.

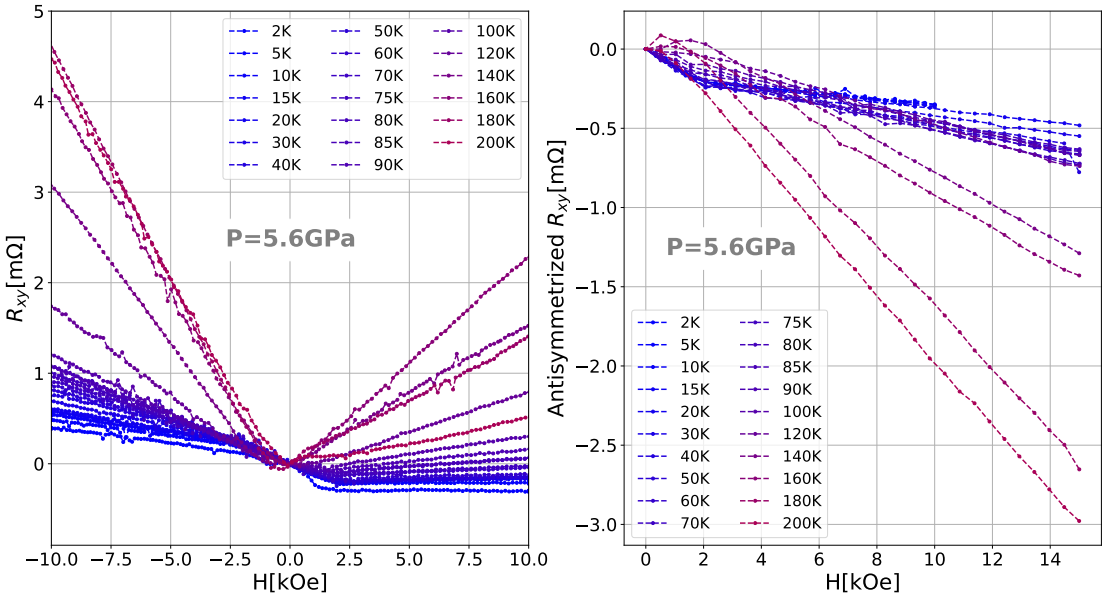

FIG. S18. The left panel displays the raw data of R_{xy} as a function of the applied field H for the second sample in the metallic state at a pressure of 5.6 GPa. The right panel shows the same data after antisymmetrization.

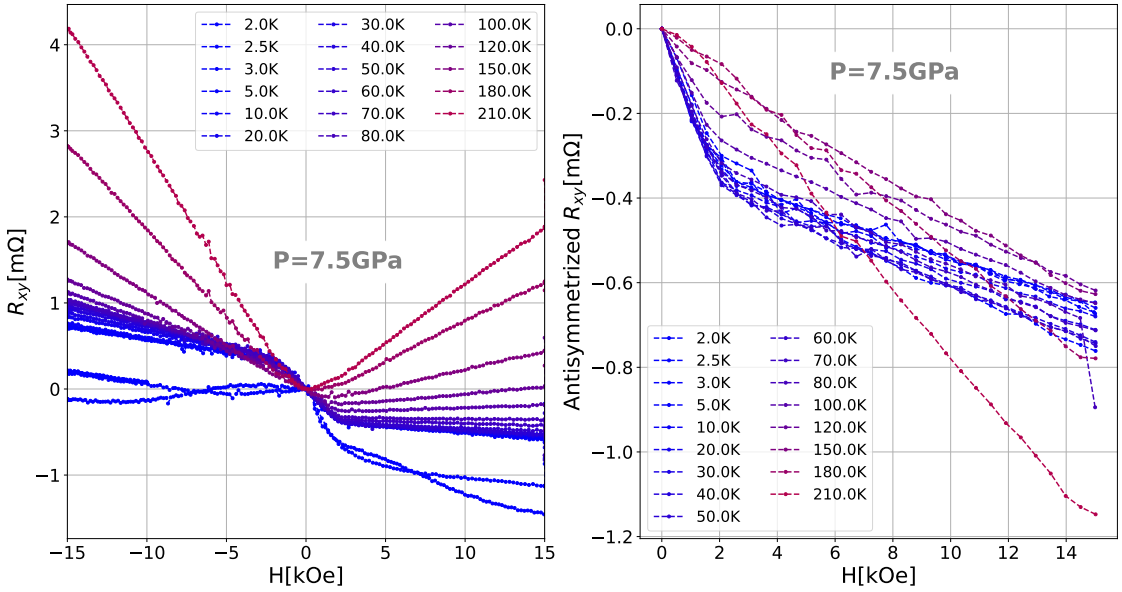

FIG. S19. The left panel displays the raw data of R_{xy} as a function of the applied field H for the second sample in the metallic state at a pressure of 7.5 GPa. The right panel shows the same data after antisymmetrization.

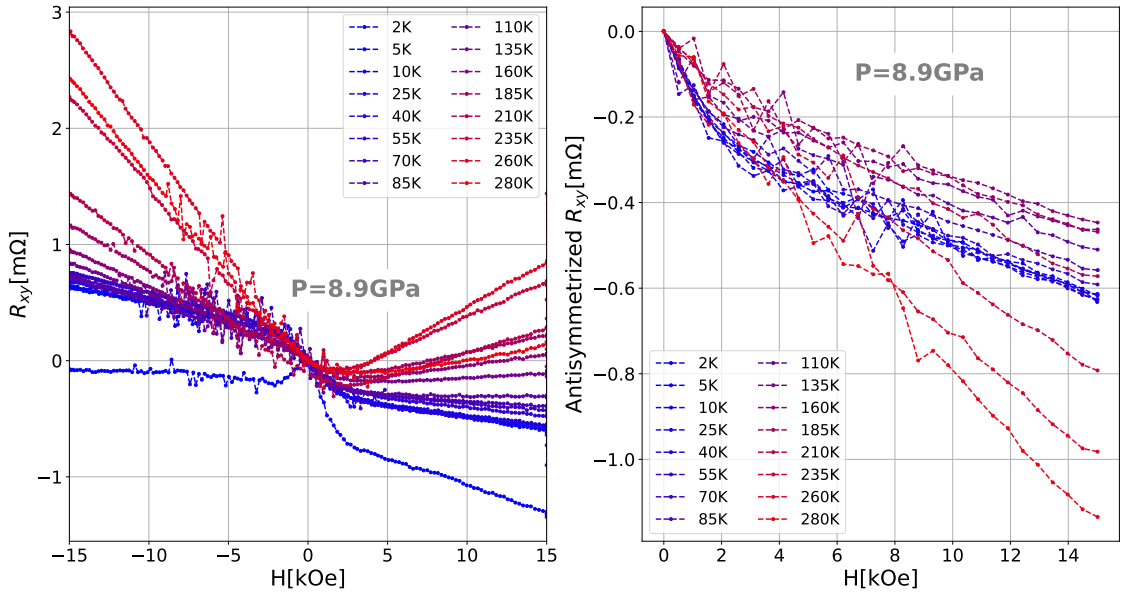

FIG. S20. The left panel displays the raw data of R_{xy} as a function of the applied field H for the second sample in the metallic state at a pressure of 8.9 GPa. The right panel shows the same data after antisymmetrization.

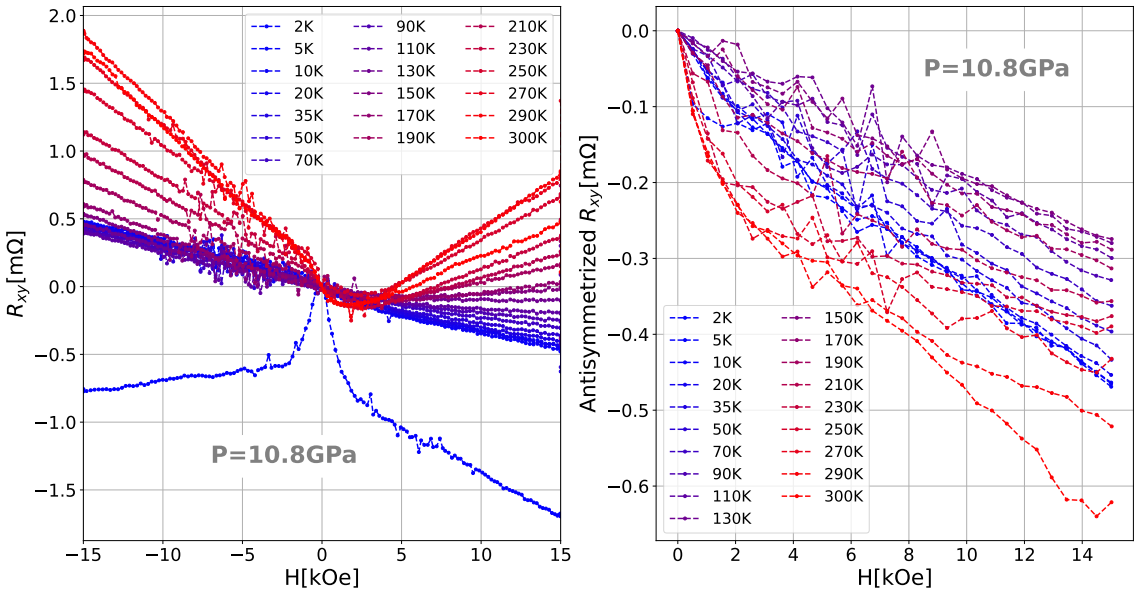

FIG. S21. The left panel displays the raw data of R_{xy} as a function of the applied field H for the second sample in the metallic state at a pressure of 10.8 GPa. The right panel shows the same data after antisymmetrization.

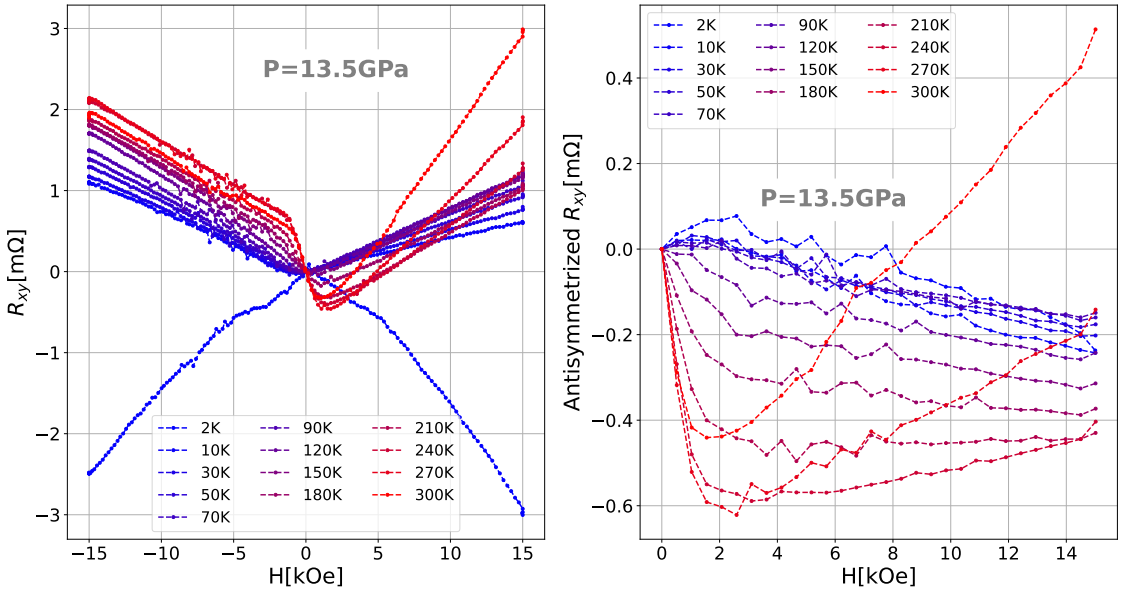

FIG. S22. The left panel displays the raw data of R_{xy} as a function of the applied field H for the second sample in the metallic state at a pressure of 13.5 GPa. The right panel shows the same data after antisymmetrization.

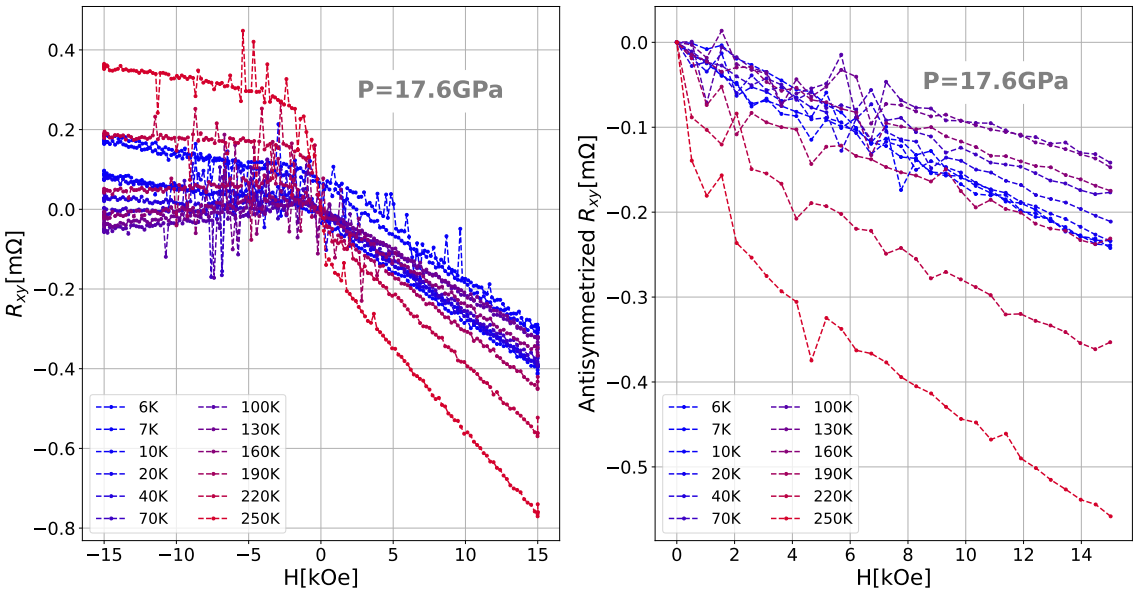

FIG. S23. The left panel displays the raw data of R_{xy} as a function of the applied field H for the second sample in the metallic state at a pressure of 17.6 GPa. The right panel shows the same data after antisymmetrization.